Journal of Alloys and Compounds 1010 (2025) 177143

Contents lists available at ScienceDirect

Journal of Alloys and Compounds

journal homepage: www.elsevier.com/locate/jalcom

Mechanical and corrosion behavior of $CoCrFeNiAl_{0.3}$ high entropy alloy seamless tubes

Yaqi Wu [a], Yuanying Yue [a], Xuehui Yan [b], Cheng Zhang [a], Jinfeng Huang [a], Peter K. Liaw [c], Yong Zhang [a,*]

[a] University of Science And Technology Beijing, State Key Laboratory for Advanced Metal Materials, Beijing 10083, China
[b] GRIMAT Engineering Institute Co., Ltd., Beijing 101407, China
[c] Department of Materials Science and Engineering, The University of Tennessee, Knoxville, TN 37996, USA

ARTICLE INFO

Keywords:
High entropy alloy
Seamless tubes
Mechanical property
Corrosion resistance

ABSTRACT

An urgent need arises for alloys that possesses superior ductility and good corrosion resistance, essential for applications in highly harsh environmental conditions. The corrosion resistance and mechanical properties of $CoCrFeNiAl_{0.3}$ high-entropy alloy seamless tubes (HEASTs) are investigated in this study. Electron Channeling Contrast Imaging (ECCI) and Electron Backscatter Diffraction (EBSD) techniques reveal the presence of abundant dislocations within the inner crystals, highlighting the alloy's excellent deformation ability. The formation of the B2 phase significantly influences corrosion behavior, with higher B2 content promoting pit propagation and enhancing pitting corrosion. Corrosion test results demonstrate the superior pitting corrosion resistance of TR-22 tubes, attributed to their lower B2 phase content and effective coverage by a protective passive film formed by Al, Cr, and Fe. X-ray photoelectron spectroscopy (XPS) analysis further elucidates the correlation between B2 phase content and corrosion resistance, emphasizing the importance of controlling B2 content to optimize microstructure. Overall, this study provides valuable insights into enhancing the corrosion resistance and mechanical properties of high-entropy alloy seamless tubes, contributing to the development of advanced materials in engineering applications.

1. Introduction

Metal tubes are widely utilized across various industries for their exceptional mechanical, chemical, and processing properties. These tubes play a crucial role in numerous applications from construction to aviation. In recent years, the increasing emphasis on energy development has underscored the importance of pipeline storage and transportation, particularly in clean energy sectors. This growing demand necessitates materials that can meet stringent requirements, driving the exploration of innovative alloys such as high-entropy alloys (HEAs).

High-entropy alloys (HEAs) represent a recent advancement in alloy development, characterized by their unique composition of multiple principal elements. This high-entropy effect results in a simple solid-solution structure, offering flexibility in adjusting strengthening phases and yielding outstanding mechanical properties. Various phases, including $L1_2$ structure γ' phase [1–7], $D0_{22}$ structure γ'' phase [8–12], B2-phase precipitates [13–15], hard σ [16–19], and intermetallic compounds [20–23] contribute to the mechanical strength of HEAs. Additionally, HEAs demonstrate notable corrosion resistance due to the role of specific elements. For instance, research by Chai et al. on face-centered-cubic (FCC) -structured FeCoNiCrx (x = 0, 0.5, 1.0) [24] alloy revealed that the passivation layer effectively prevents corrosive agents, such as Cl^- ions, from penetrating the base metal, thereby enhancing corrosion resistance of alloys. Ni provides excellent oxidation and corrosion resistance in alloys, particularly in acidic and alkaline environments [25], while Co synergistically enhances overall corrosion resistance when combined with nickel and chromium (Cr). Moreover, aluminum (Al), despite its controversial role, can form a protective Al_2O_3 passivation film in oxidizing environments [26,27], albeit prone to localized corrosion (pitting) in chloride-containing environments. However, the inclusion of Mo in aluminum-containing alloys has been shown to effectively mitigate pitting corrosion issues. These findings underscore the potential of HEAs to not only deliver superior mechanical properties but also to withstand corrosive environments, making them promising candidates for applications in sectors such as transportation, infrastructure, and marine engineering. By harnessing the

* Corresponding author.
E-mail address: drzhangy@ustb.edu.cn (Y. Zhang).

https://doi.org/10.1016/j.jallcom.2024.177143
Received 13 June 2024; Received in revised form 17 September 2024; Accepted 17 October 2024
Available online 18 October 2024
0925-8388/© 2024 Elsevier B.V. All rights are reserved, including those for text and data mining, AI training, and similar technologies.

synergistic effects of the alloy composition, HEAs offer a compelling solution to address the dual challenges of mechanical strength and corrosion resistance in demanding operating conditions.

Despite the promising properties of HEAs, research in this field has been limited, primarily due to challenges related to high strength and work hardening. Among various HEA systems, the FCC $CoCrFeNiAl_{0.3}$ HEA [28], reinforced by nano-precipitate phases, displays external work-hardening properties and favorable processing characteristics. It possesses excellent capacity of deformation in the room temperature and outstanding fracture toughness in the cryogenic temperature [29,30], which are potential for being applied at wide temperature range.

Previous works have demonstrated that $CoCrFeNiAl_{0.3}$ outperforms conventional materials like 316 L steel [31,32] in terms of corrosion resistance. This competitive advantage positions $CoCrFeNiAl_{0.3}$ HEA as a promising candidate for the fabrication of seamless pipes, particularly for use in cryogenic, high-pressure, and corrosive environments. Thus, there is an opportunity to achieve an optimal balance between mechanical properties and corrosion resistance.

This investigation focuses on exploring the mechanical properties of HEAs across different tube diameters and their corrosion resistance within a 3.5 % NaCl solution environment. By examining high-entropy alloy seamless tubes (HEASTs), this study aims to significantly expand the scope of research in this field, providing valuable insights for future applications.

2. Experiment preparation

2.1. Samples production

The samples were prepared from forged Φ44×600 mm (diameter × length) rods of our prior work. Initially, the Φ44×600 mm rods undergo annealing and softening at 1100°C for 90 min, followed by piercing to create primary Φ44×7 mm (diameter × thickness) tube blanks. These primary tube blanks are then cold-rolled to form Φ34.5×4.5 mm cold-rolled tubes. Subsequently, the annealing, softening, and cold rolling processes are repeated to produce seamless tubes with the sizes of Φ25×3 mm, Φ22×2 mm, and Φ10×1 mm. Following each cold rolling step, the tubes undergo bright annealing, softening, straightening, and pickling to ensure a smooth surface finish.

2.2. Characterization and analysis of specimens

The phase composition of seamless tubes was determined by a Smart Lab 9 kW X-ray diffraction (XRD) system with Cu-α radiation, followed by microstructure characterization using scanning-electron microscope (SEM) with a ZEISS Gemini 450 operated at 20 keV, along with electron microscopy energy spectrometer (EDS). The grains in the tubes were analyzed using electron backscatter diffraction (EBSD), and their texture was represented by inverse pole figures (IPFs) corresponding to the deformation direction. To further investigate the dislocation and strengthen mechanical of tubes, the deformed microstructure was also conducted by electron channeling contrast imaging (ECCI) and high-resolution transmission electron microscopy (TEM) with a JEM-2010. Two-step polishing methods made the TEM samples. The TEM samples were first mechanically ground to a thickness of 40 μm, then twin-jet electro-polished with a solution of $HClO_4$:C_2H_5OH=1:9.

2.3. Mechanical and corrosion performance testing

Tensile test at a strain rate of 1×10^3 s^{-1} at 298 K, using WDW-200D microcomputer controlled electronic universal testing machine with a sample gauge length of 50 mm. To assess corrosion resistance, electrochemical testing was performed with the Gamry Reference 600 + electrochemical comprehensive tester. Additionally, the composition of corrosion products was investigated through X-ray photoelectron spectroscopy (XPS, Thermo-Scientific), with Al Kα (1486.6 eV, 150 W) serving as the X-ray source. XPS spectra was analyzed via Advantage software.

3. Results

3.1. Phase and Microstructure Evolution of High-Entropy Alloy Seamless Tubes

The phase and microstructures of the high-entropy alloy seamless tubes (HEASTs) are illustrated in Fig. 1. Fig. 1(a) provides picture of seamless tube, with the cross-sectional sizes from Φ44×7 mm to Φ10×1 mm. EDS maps (Fig. 1b) reveal that all the alloying elements (Al, Co, Cr, Fe, Ni) distribution, with the Al segregation in the grain boundaries. As given by Table 1, shows the compositions of each tube. The X-ray diffraction patterns of $CoCrFeNiAl_{0.3}$ seamless tubes undergoing cold rolling and annealing processing are depicted in Fig. 1(c), revealing the presence of a single FCC crystal structure as the main phase. The Al-rich phase is confirmed by TEM as B2, and Fig. 1(d) shows the microstructure and selected area electron diffraction (SAED) patterns.

Fig. 2(a-c) delineate the grain-size diagram, with the inverse pole figures inserting. Following annealing at 1100°C for 90 minutes, $CoCrFeNiAl_{0.3}$ HEASTs of diverse specifications exhibit nearly completed recrystallization. Increased rolling deformation corresponds to a reduction in the average annealed grain size. Specifically, TR-25 exhibits an average grain size of 35.7 μm, TR-22 has an average grain size of 33.1 μm, and TR-10, experiencing the highest deformation, has a grain size of 29.4 μm, indicating significant grain refinement. Moreover, B2 precipitation is primarily found in the grain boundaries (GBs), as seen in Fig. 2 (e-f). The B2 phase contents of TR-25, TR-22 and TR-10 HEASTs are 0.4 %, 0.29 % and 1.17 %, respectively.

3.2. Tensile behavior and fracture microstructure

Fig. 3(a) displays the engineering stress-strain curves of HEASTs tested at 298 K, showing the tensile ductility also dropped from 48 % to 35.8 %, while yield strength increased and ultimate tensile strength was reduced, from 279 to 308 MPa and from 680 to 610 MPa, respectively. The higher yield strength of TR-10 is caused by its smaller grain size and higher B2 phase composition. Overall, it seems that HEASTs exhibit a monotonically reduced strain hardening rate (SHR, θ) until the final instable failure. However, the strain hardening curves of HEASTs display a small profile of up-turn in the range of ~0.1 to ~0.3. The similar phenomenon was also reported in other HEAs with low stacking faults energy which is generally related to the transition of deformation mechanism. Compared with the strain hardening behavior of TR10, the TR-25 and TR-22 possess a slightly higher strain hardening capability with larger uniform elongation (35.8 %). Serrated fluctuation in the SHR curve is caused by the dynamic strain failure of the alloy, which has been reported in many literatures and will not be discussed in this paper.

Fig. 4(a) displays the fracture morphologies of samples tested at 298 K. The observation reveals the ductile dimples in both specimens, further supporting the good plasticity. Additionally, the difference is that the dimples of TR-10 are shallower, as compared to the other two, which is consist the plasticity values in all specimens.

3.3. Potentiodynamic polarization test and microstructure of the corrosion surface

Table 1 displays the potentiodynamic polarization test results. The polarization curve is used to evaluate the alloy's resistance to corrosion. Better corrosion resistance of the alloy is indicated by lower corrosion current density (I_{corr}) and greater polarization voltage (E_{corr}). Additionally, a higher pitting potential (E_{pit}) suggests better resistance to pitting corrosion. Table 1 displays E_{corr}, I_{corr}, E_{pit}, and R_p values of tubes in a 3.5 wt% NaCl solution. It is observed that as the proportion of B2

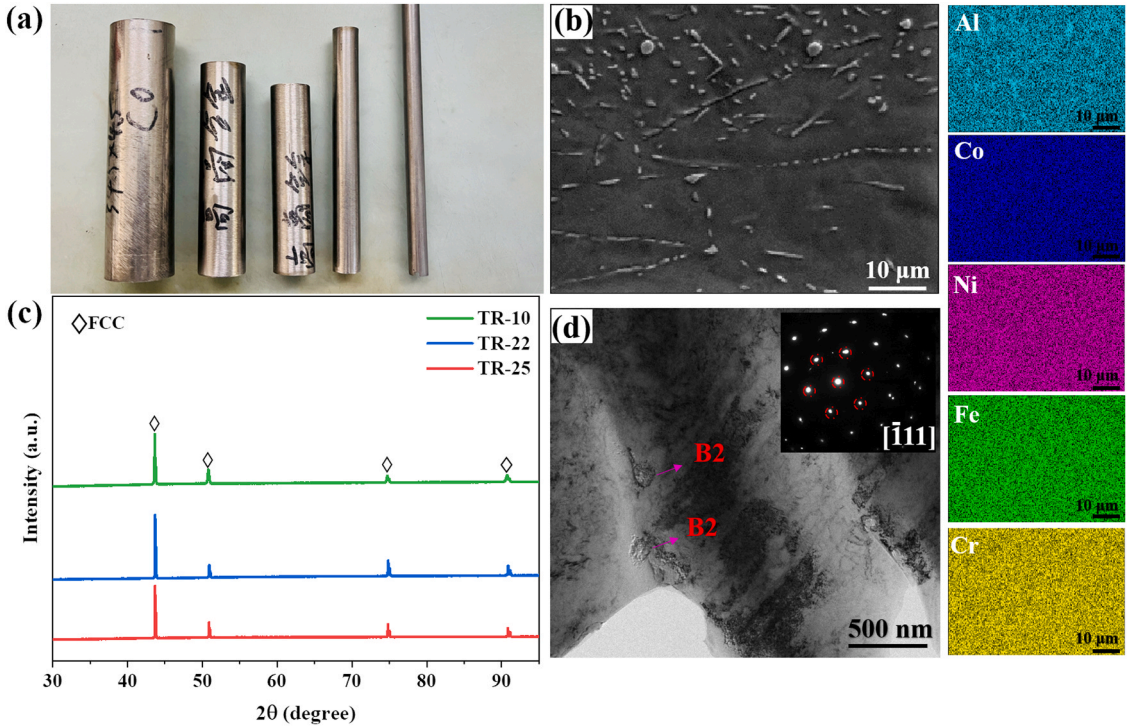

Fig. 1. The morphologies and structures of HEASTs. (a) The macroscopic views of STs with various diameters, as followed by TR-44: Φ44×7 mm; TR-34.5: Φ34.5×4.5 mm TR-25: Φ25×3 mm; TR-22: Φ22×2 mm; and TR-10: Φ10×1 mm; (b) SEM-EDS maps showing the distribution of Al, Co, Cr, Fe, Ni of initial specimens; (c) The XRD pattern for samples; (d) Bright filed TEM image the SAED pattern for B2 phase.

Table 1
Chemical compositions (at%) of tubes.

Tubes/elements(at%)	Al	Co	Cr	Fe	Ni
TR−25	7.79	22.26	22.85	22.77	24.33
TR−22	7.38	23.09	24.27	22.14	23.12
TR−10	6.82	22.99	23.22	23.29	23.68

phase increases, the average R_p increases, and both E_{pit} and I_{corr} decrease. This indicates a negative correlation between R_p and E_{pit}, and a positive correlation between I_{corr} and the content of the B2 phase, respectively. These findings suggest that the B2 phase can worsen passivation and facilitate pitting corrosion. Table 2

Fig. 5 presents Tafel curves of HEASTs samples in a 3.5 wt% NaCl solution. The anodic curves demonstrate a direct transition from the corrosion potential to the stable passive region, indicating spontaneous passivation of all the samples in the solution. As the potential further increases, the current density (I_{corr}) rises rapidly, signifying the occurrence of stable pitting corrosion, and such a potential is usually regarded as the pitting potential (E_{pit})↱ [33,34]. Fig. 5(b) compares the obtained I_{corr} and E_{pit}. Corrosion current density I_{corr} and polarization R_p can be obtained from Tafel equation ↱[35]:

$$I_{corr} = \frac{I}{\exp(\frac{\beta(E-E_{corr})}{0.0591})} \quad (1)$$

$$Rp = \frac{0.0591}{i_{corr}} \quad (2)$$

where, I (A/cm^2) is anode current, I_{corr} (A/cm^2) is corrosion current density, E is potential, β is slope of anode Tafel curve, and 0.0591 is the conversion factor that converts the base e of the natural logarithm to the base 10 of the common logarithm. It is noticed that R_p increases and E_{pit} and I_{corr} decrease when the proportion of B2 phase increasing. In other words, R_p correlate negatively with the content of the B2 phase while E_{pit} and I_{corr} correlate positively. It demonstrates that the B2 phase can worsen passivation and facilitate pitting corrosion.

3.4. X-ray photoelectron spectroscopy

The surface analysis of passive films was conducted, using the X-ray photoelectron spectroscopy as shown in Fig. 6. The presence of various elements and their oxidation states were detected and analyzed. The C peak detected at 284.8 eV might be attributed to external contamination, while the presence of O indicates oxidation of the metal surface, forming corresponding oxides and hydroxides. According to the XPS database, Al 2p spectra show the presence of Al (72.6 eV) and Al^{3+} (75.6 eV). The Co 2p3/2 spectra reveal metallic Co-metal (777.8 eV), Co^{2+} (780.5 eV), Co^{3+} (783.1 eV), and Co^{2+}_{sat} (786.2 eV), attributed to monopole charge-transfer transitions. Similarly, the Cr 2p3/2 spectra exhibit the Cr 2p3/2 spectra exhibit Cr-metal (573.6 eV), Cr^{3+}_{ox} (576.1 eV), and Cr^{3+}_{hy} (577.3 eV). The Fe 2p3/2 spectra display metallic Fe^{2+} (707.6 eV), Fe^{3+} (710.0 eV), and Fe^{3+} (712.6 eV), while the Ni 2p3/2 spectra consist of Ni-metal (852.4 eV), Ni^{2+}_{ox} (853.8 eV), and Ni^{2+}_{hy} (855.8 eV). At low passive potentials, water (H_2O) is adsorbed on the metal surface according to chemical reactions (3)-(5).↱[36]:

$$H_2O(aq) + M \rightarrow H_2O + M \quad (3)$$

$$H_2O(aq) + MOH \rightarrow M + H^+(aq) + e^- \quad (4)$$

$$H_2O(aq) + MO \rightarrow M + 2H^+(aq) + 2e^- \quad (5)$$

With increasing passive time, partial metal hydroxides ($M(OH)_x$) are dehydrated to form dense metal oxides (M_xO_y), which play a major role in the protective properties of the passive film.

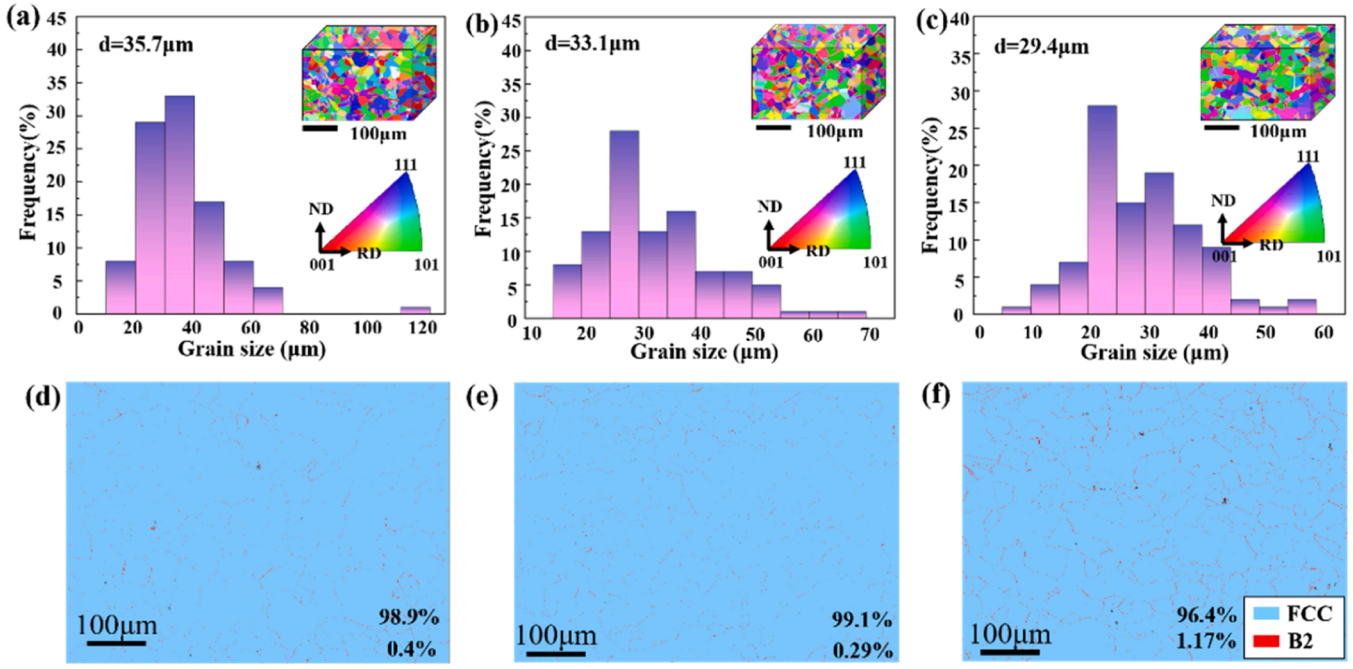

Fig. 2. EBSD diagram of (a) TR-25; (b) TR-22; and (c) TR-10 HEASTs after annealing. The invers polar figures are inserted in the right-up corner; (c-f) phase distribution and percentage of HEASTs.

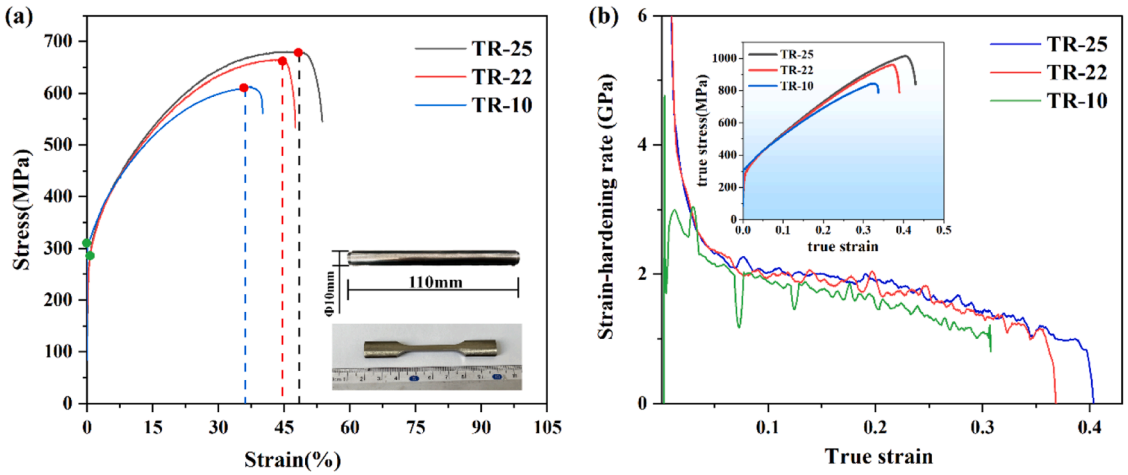

Fig. 3. Tensile properties of $CoCrFeNiAl_{0.3}$ HEASTs at 298 K. (a) Engineering strain-stress curves; (b)True stress-strain curves and correspond strain-hardening rates of HEASTs.

4. Discussion

4.1. Deformation mechanisms

Fig. 7 According to the above mechanical results and fracture morphology, it can be concluded that the difference in properties is closely related to the microstructure. In order to further analyze the difference, the mechanism was discussed by TEM. B2 phase reinforcement is a common way of FCC high intensity, in many systems of FCC [13–15]. According to the results of EBSD (Fig. 2d-f), the TR-10 has a larger content of B2 than the TR-25 and the TR-22, and while the difference in content is modest, it produces changes in yield strength. The TEM characterization of TR-10 after 20 % strain confirms the dislocations pinning-up by the B2 phase in the GBs, as shown in Fig. 8. In Fig. 8 (c), the dislocations are obstructed by GBs, except for B2 particles.

Besides the dislocation slipping, the twinning is another plastic deformation mechanism of materials. The TEM image as well as its selected SAED pattern also confirms the existence of deformation twins, as shown in Fig. 9(a) and (b). After tension deformation, the twin boundary acts as the barrier to dislocation movement and eventually produces the dislocation bands near two sides of a twin [37] The bright- and dark-field TEM images (Fig. 9(c) and the inset) reveal several thin deformation twins, as evidenced by the SAED pattern. When the deformation twins form, the dislocation movement will be hindered by the twin boundaries. The role of twin boundaries is similar to that of grain boundaries. This means that the deformation twins will decrease the mean free path of dislocation, eventually enhancing the strength through dynamic Hall-Petch effect [38,39]. On the other hand, the twinning can active the ne slipping systems and promote more dislocation slipping when the original dislocations are hindered by twin boundaries. Besides, the twins can also accommodate more dislocations and enhance the dislocation storage capacity, and thus improve the

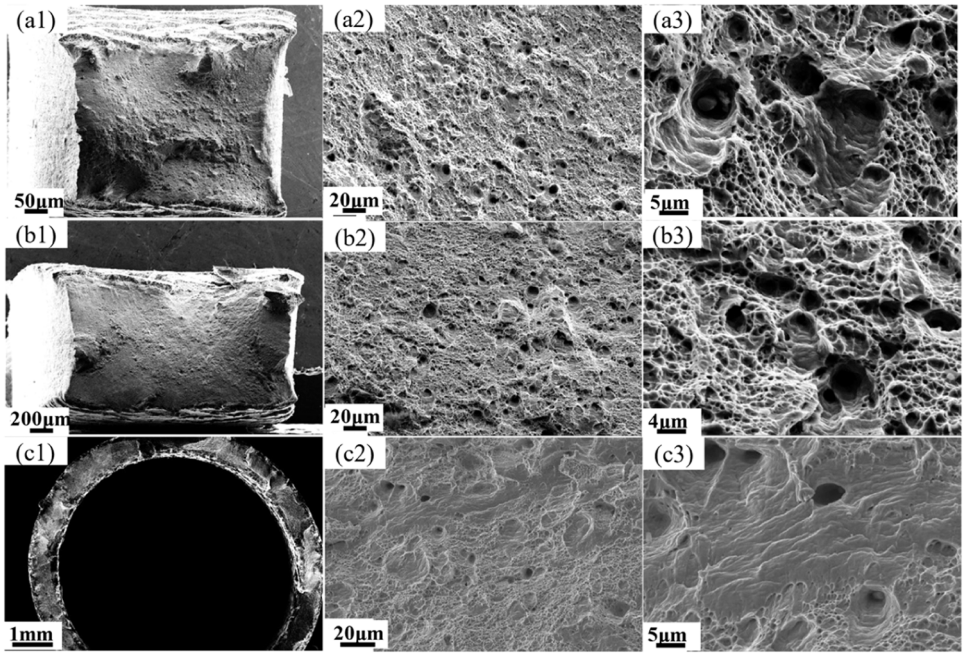

Fig. 4. The fracture topographies of (a)TR-25, (b)TR-22, and (c)TR-10 HEASTs.

Table 2
E_{corr}, I_{corr}, E_{pit} and R_p of tubes in 3.5w.t % NaCl solution.

Alloys	E_{corr}(mV)	I_{corr}(μA/cm^2)	E_{pit} (mV)	R_p
TR−25	−0.2079-	0.2126	0.173	0.2779
TR−22	−0.2327	0.2389	0.292	0.2473
TR−10	−0.1968	0.0625	0.035	0.9456

plasticity ↱[40,41]. Based on above results and analyses, the role of deformation twins and refined grains in the dislocation motion is probably the main reason for the good balance of strength and ductility in the TR-25 and TR-22 HEASTs. However, dense and narrow parallel single nanotwins (Fig. 9d-g), even the multiple-twins emitted from the matrix interface were observed in deformed TR-10 specimens. Narrow twin bands offer more interface, making dislocations difficult to pass through and limiting the plasticity of the material. Obviously, the above twinning-related processes significantly contribute to the enhanced strain hardening capacity of HEASTs at both temperatures.

In particular, multiple-twinning at TR-25 and TR-25 confers more sustainable strain hardening in the stretched sample ↱[42]. Meantime, compared with narrow twins, multiple-twins observed sample can further lead to more pronounced strain-hardenability of materials, which is consist with the corresponding SHR.

4.2. Corrosion resistance

The corrosion test results demonstrate that TR-22 tubes exhibit superior pitting corrosion resistance, correlating well with their lower B2 phase content ↱[43,44]. The corrosion test results demonstrate that TR-22 tubes exhibit superior pitting corrosion resistance, correlating well with their lower B2 phase content.

Al, being more reactive than Fe, Co, Ni, and Cr, tends to dissolve preferentially in a corrosive environment, forming a protective passivation film that acts as a barrier to corrosion. Consequently, the AlNi-rich and Cr-depleted B2 phase becomes a preferred site for initiating pitting

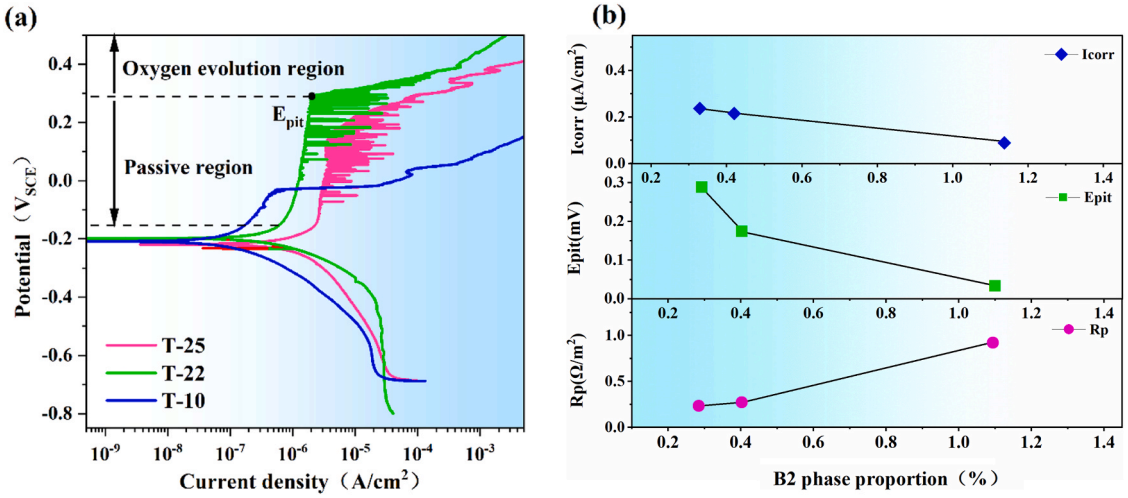

Fig. 5. (a) Polarization curves of $CoCrFeNiAl_{0.3}$ HEASTs with different specifications in the 3.5 wt% NaCl solution;(b) Variation of polarization resistance (R_p), corrosion current density (I_{corr}) and pitting potential (E_{pit}) of the annealed $CoCrFeNiAl_{0.3}$ HEASTs in 3.5 wt% NaCl solution.

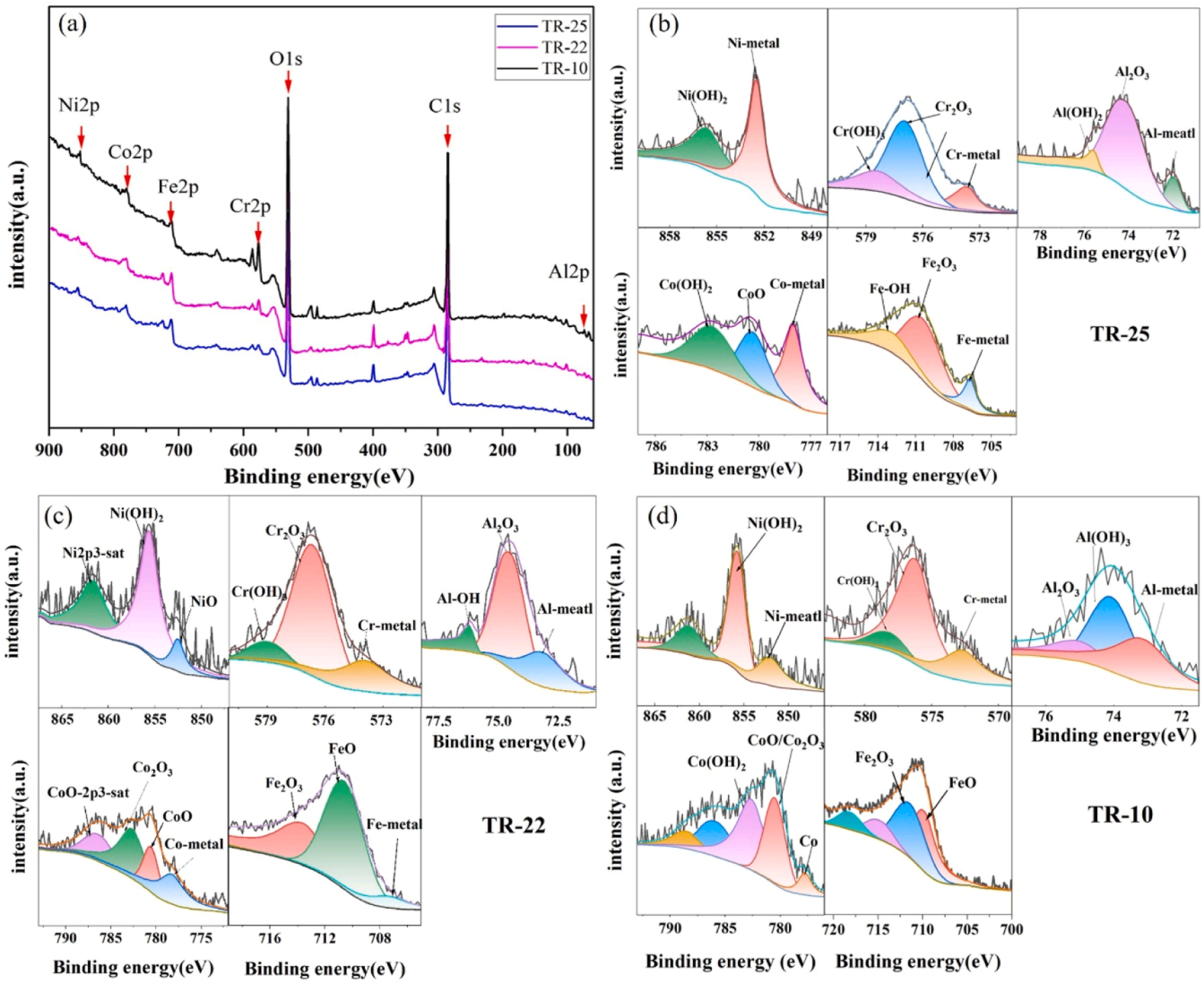

Fig. 6. (a)The XPS spectra of the passive films formed on STs. (b) displays the spectra of TR-25 STs; (c) are the protection result of TR-22 STs; (d) present the XPS spectra of TR-10 STs.

corrosion [45]. Moreover, the presence of Cl^- ions further exacerbates corrosion by promoting competitive adsorption and permeation [46,47]. The resulting chemical reaction couple, facilitated by the high-energy interface of the precipitated phase, accelerates the corrosion process. The metal ions ionized into solution and combined with OH^- to form coordination complex ($(MOH)_x$, M = Fe, Ni, Cr, Co, Al) at GBs, as followed chemical reaction:

$$O_2 + 2H_2O + 4e^- \rightarrow 4OH^- \quad (6)$$

$$M + 2Cl^- \rightarrow MCl_2 + 2e^- \quad (7)$$

Cl^- ions migrate to this interface, thereby promoting the corrosion process [48,49], as depicted by yellow balls and purple arrow in right up side of Fig. 9(a). The surface of TR-22 sample, with fewer pitting nucleation sites, is primarily covered by the protective passive film formed by Al, Cr, and Fe in the matrix, preventing further corrosion, as shown in Fig. 9(b).

A semi-quantitative examination of elemental composition and oxide formation using X-ray photoelectron spectroscopy (XPS) clarifies the correlation between B2 phase concentration and corrosion resistance. As shown in Fig. 10, the variation in Al, Cr, Ni, Co, and their oxides are indicated individually. During passivation, aluminum readily generates aluminum oxide (Al_2O_3) or aluminum hydroxide ($Al(OH)_3$). As the B2 phase concentration increases, the presence of Al-rich area causes to more Al to be oxidized, resulting in the formation of additional Al_2O_3 or $Al(OH)_3$ in the passivation film. Increased B2 content reduces the quantity [22,43,44,50,51]. Reduced Cr-rich areas lead to increased B2 distribution along GBs, resulting in more severe pitting and decreased pitting potential [52]. Furthermore, when the B2 level rises, the proportion of oxides of elements such as Ni and Co, which are less prone to corrosion, gradually increases in the passive layer. It suggests a deeper level of pitting corrosion, which results in the progressive production of a passive film within the sample. The dynamic variations in elemental oxides with varied B2 concentration highlight the necessity of regulating the B2 phase content to maximize microstructure and corrosion resistance in the $CoCrFeNiAl_{0.3}$ alloy.

5. Conclusion

In conclusion, this work sheds light on the mechanical properties and corrosion resistance of $CoCrFeNiAl_{0.3}$ HEASTs across various pipe diameters in a 3.5 % NaCl solution. Our findings emphasize the exceptional mechanical properties of the tubes, which is principally related to work-hardening and precipitation-strengthening mechanisms.

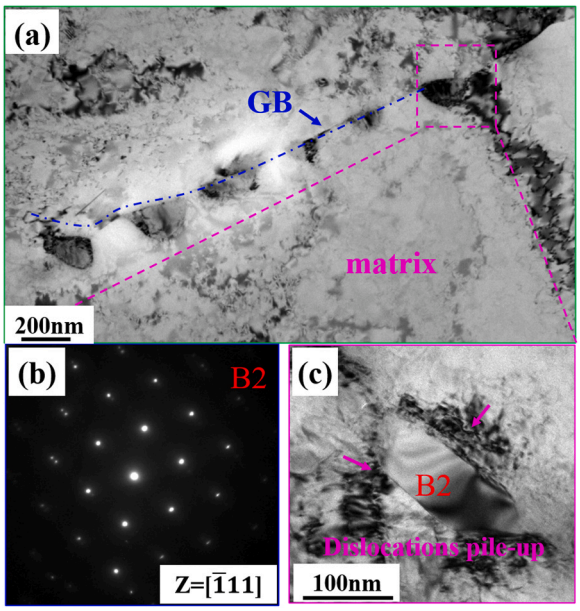

Fig. 7. The TEM images of TR-10 tube after 20 % strain. (a) A TEM image showing B2 particles distribute at the GBs, and it SAED pattern; (c) The enlarged image of dislocations pinned by B2 particle.

However, it highlights the significant impact of precipitates in impeding the improvement of corrosion resistance.

(1) The outstanding comprehensive mechanical properties of STs with different diameters result from abundant dislocations, deformed-twining and precipitation-phase strengthening.

(2) Density deformed twinning endows the excellent ductility, more sustainable strain hardening, and lead to more pronounced strain-hardenability.

(3) The corrosion resistance of the seamless tubes is notably influenced by the ratio of the B2 phase. Notably, the TR-22 STs exhibit the least presence of the B2 phase, correlating with superior pitting resistance. Remarkably, despite the reduced B2 phase content, the mechanical properties of these tubes demonstrate a tensile strength of 650 MPa, showcasing an optimal balance between mechanical robustness and corrosion resistance across the three pipe specifications.

This study not only indicates the first examination of high-entropy alloy seamless tubes but also provides valuable insights into the development of advanced materials tailored for harsh environmental conditions. By advancing our understanding of the interplay between microstructure, corrosion resistance, and mechanical properties, this research contributes to the ongoing quest for innovative materials with enhanced performance and durability in engineering applications.

Funding

Yong Zhang acknowledges supports from: (1) National Natural Science Foundation of China (No. 52273280), (2): Mechanism Research and Preparation Technology of High Entropy Alloys with Ultra-high Strength (No. 2020–0531), and (3) Creative Research Groups of China (No. 51921001). Peter K. Liaw very much appreciates the support from (1) the National Science Foundation (DMR – 1611180, 1809640, and 2226508) and (2) the US Army Research Office (W911NF-13–1–0438 and W911NF-19–2–0049). Xuehui Yan acknowledges the financial supports from the Youth Fund Project of GRINM (No.66922309) and National Natural Science Foundation of China (No.52301220).

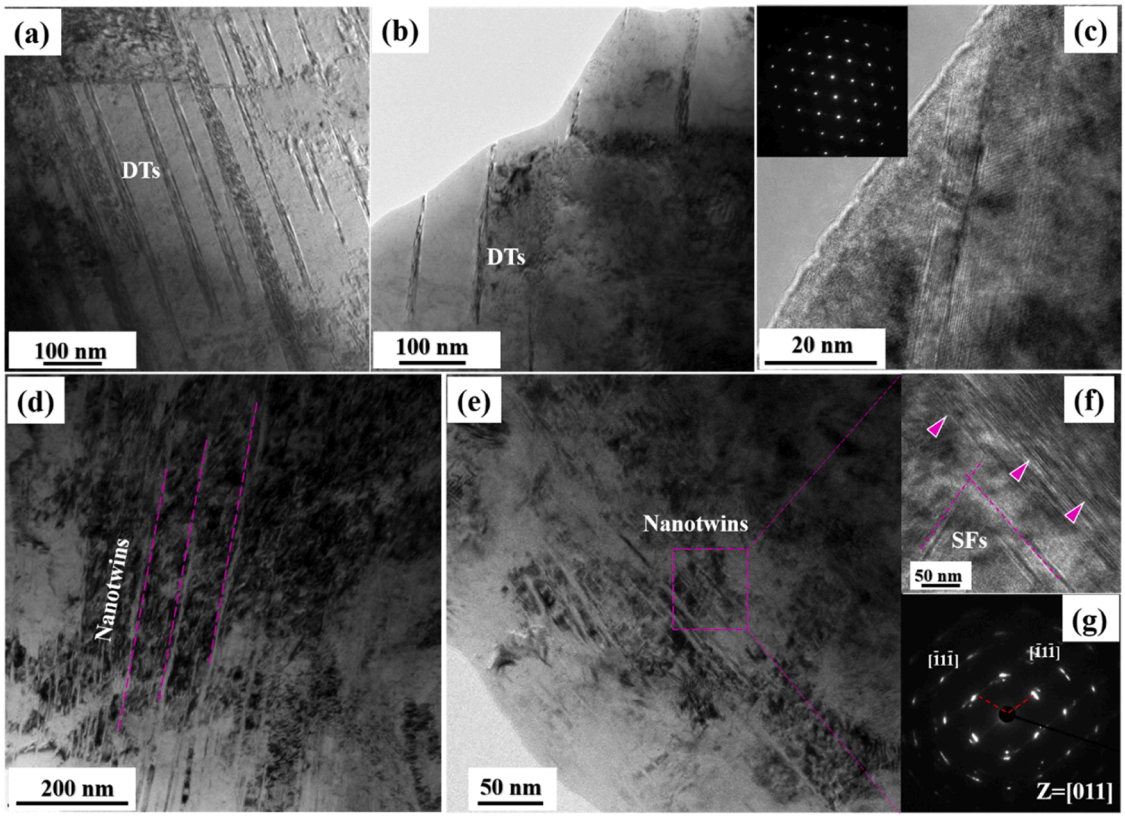

Fig. 8. The microstructures of HEASTs. (a) A TEM image showing deformed twins and stacking faults (SFs). (b) and (c) shows the deformed twins and their HRTEM image of TR-22 tubes; The parallel nanotwins in the TR-10 samples.

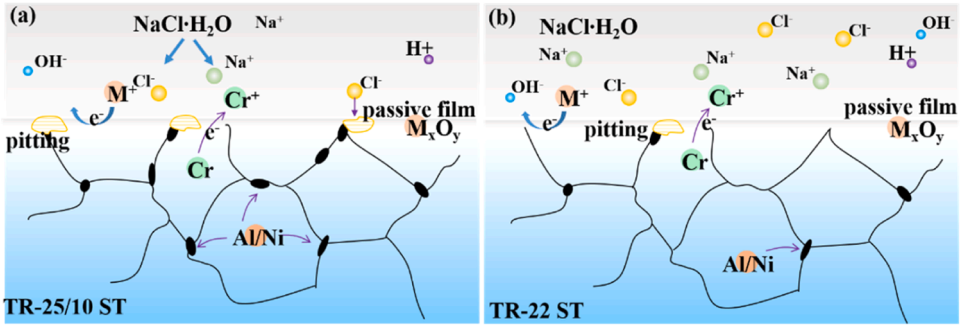

Fig. 9. The diagram of corrosion behaviors of samples in the 3.5 % NaCl solution. (The purple arrow shows the direction of the atom's diffusion. The brown ellipse represents the B2 phase.).

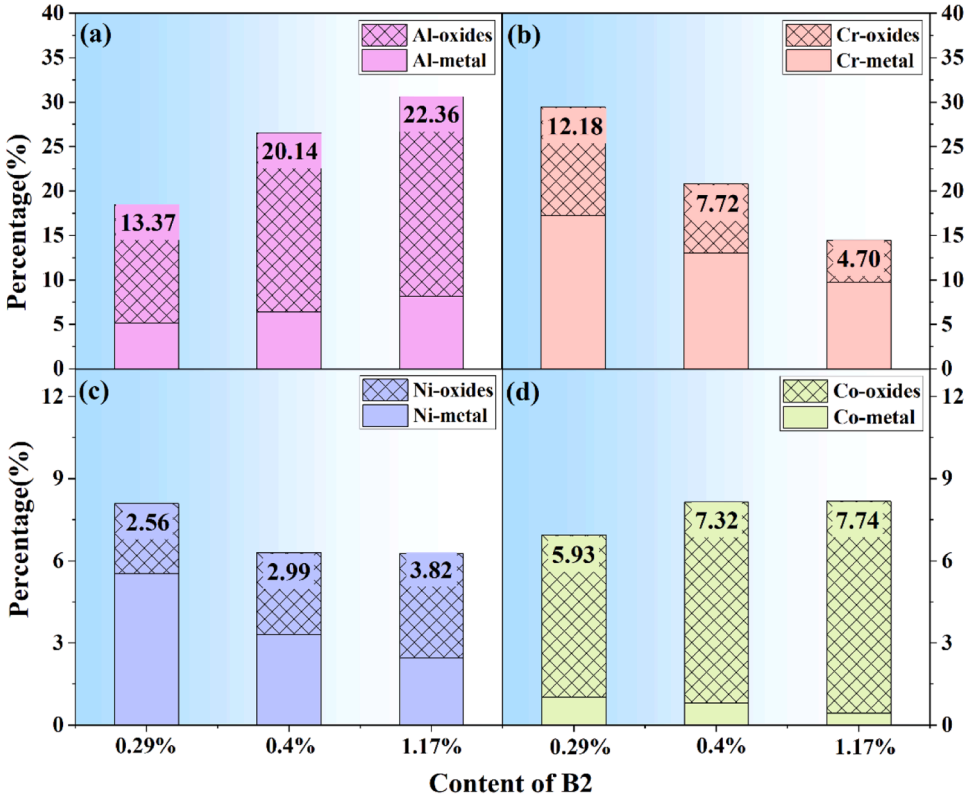

Fig. 10. The variation of elements and their oxides in the passive film with B2 content.

CRediT authorship contribution statement

Cheng Zhang: Supervision. **Xuehui Yan:** Supervision. **Yong A Zhang:** Supervision, Conceptualization. **Peter K. Liaw:** Supervision. **Jinfeng Huang:** Supervision. **Yaqi Wu:** Writing – original draft, Methodology, Investigation. **Yuanying Yue:** Methodology, Investigation.

Declaration of Competing Interest

The authors declare that they have no known competing financial interests or personal relationships that could have appeared to influence the work reported in this paper.

Data Availability

No data was used for the research described in the article.

References

[1] Y.L. Zhao, T. Yang, Y.R. Li, L. Fan, B. Han, Z.B. Jiao, D. Chen, C.T. Liu, J.J. Kai, Superior high-temperature properties and deformation-induced planar faults in a novel L12-strengthened high-entropy alloy, Acta Mater. 188 (2020) 517.
[2] W.J. Lu, X. Luo, T.Q. Yang, K. Yan, B. Huang, P.T. Li, Nano-precipitates strengthened non-equiatomic medium-entropy alloy with outstanding tensile properties, Mat. Sci. Eng. 780 (2020) 139218.
[3] L. Fan, T. Yang, J.H. Luan, Z.B. Jiao, Control of discontinuous and continuous precipitation of γ′-strengthened high-entropy alloys through nanoscale Nb segregation and partitioning. J. Alloy. Compd. 832 (2020) 154903.
[4] H.X. Yang, J.S. Li, X.Y. Pan, W.Y. Wang, H.C. Kou, J. Wang, Nanophase precipitation and strengthening in a dual-phase Al0.5CoCrFeNi high-entropy alloy, J. Mater. Sci. Technol. 72 (1) (2021).
[5] Y. Chen, H.W. Deng, Z.M. Xie, M.M. Wang, J.F. Yang, T. Zhang, Y. Xiong, R. Liu, X. P. Wang, Q.F. Fang, C.S. Liu, Tailoring microstructures and tensile properties of a precipitation-strengthened (FeCoNi)94Ti6 medium-entropy alloy, J. Alloy. Compd. 828 (2020) 154457.
[6] T. Yang, Y.L. Zhao, J.H. Luan, B. Han, J. Wei, J.J. Kai, C.T. Liu, Nanoparticles-strengthened high-entropy alloys for cryogenic applications showing an exceptional strength-ductility synergy, Scr. Mater. 164 (2019) 30.

[7] K. Górecki, P. Bala, W. Bednarczyk, J. Kawałko, Cryogenic behavior of the Al5Ti5Co35Ni35Fe20 multi-principal component alloy, Mat. Sci. Eng. 745 (2019) 346.
[8] W.J. Lu, X. Luo, Y.Q. Yang, W. Le, B. Huang, P.T. Li, J. Alloy. Compd. 833 (2020) 155074.
[9] R. Cozar, A. Pineau, Influence of the co/ni ratio on the γ and γ" precipitation in Fe-Ni-Co-Ta alloys, Metall. Trans. 5 (1974) 2471.
[10] X.Y. Gao, R. Hu, G.L. Luo, The effect of Ti on precipitation of fully coherent DO22 superlattice in an Ni-Cr-W-based superalloy, Scr. Mater. 134 (2017) 15.
[11] A. Suzuki, M. Takeyama, Formation and morphology of Kurnakov type D022 compound in disordered face-centered cubic γ-(Ni, Fe) matrix alloys, J. Mater. Res. 21 (2006) 21.
[12] K. Kusabiraki, H. Komatsu, S. Ikeuchi, Lattice constants and compositions of the metastable Ni3Nb phase precipitated in a Ni-15Cr-8Fe-6Nb alloy. Metall, Mater. Trans. 29 (1998) 1169.
[13] S. Dasari, A. Jagetia, Y.-J. Chang, V. Soni, B. Gwalani, S. Gorsse, A.-C. Yeh, R. Banerjee, Engineering of multi-scale B2 precipitation in a heterogeneous FCC based microstructure to enhance the mechanical properties of a Al0.5Co1.5CrFeNi1.5 high entropy alloy, J. Alloy. Compd. 830 (154707) (2020).
[14] X. Jin, Y.X. Liang, L. Zhang, J. Bi, Y. Zhou, B.S. Li, Back stress strengthening dual-phase AlCoCr2FeNi2 high entropy alloy with outstanding tensile properties, Mat. Sci. Eng. A. 745 (2019) 137.
[15] S. Wang, Y.H. Zhao, X.T. Xu, P. Cheng, H. Hou, Evolution of mechanical properties and corrosion resistance of Al0.6CoFeNiCr0.4 high-entropy alloys at different heat treatment temperature, Mater. Chem. Phys. 244 (2020) 122700.
[16] L. Zhang, X.F. Huo, A.G. Wang, X.H. Du, L. Zhang, W.P. Li, N. F. Lu Zhang a, Xiaofeng Huo, Anguo Wang, Xinghao Du, Li Zhang, Wanpeng Li, Naifu Zou, Gang Wan, Guosheng Duan, Baolin Wu, A ductile high entropy alloy strengthened by nano sigma phase, Intermetallics 122 (2020) 106813.
[17] Zhihan Chen Yu Yin, Damon Kent Ning Mo, Kai En. Koey Adhitya Riadhi Candella, Qi yang Tan, Michael Bermingham, Ming-Xing Zhang, High-temperature age-hardening of a novel cost-effective Fe45Ni25Cr25Mo5 high entropy alloy, Mat. Sci. Eng. 788 (2020) 139580.
[18] M.V. Klimova, D.G. Shaysultanov, S.V. Zherebtsov, N.D. Stepanov, Effect of second phase particles on mechanical properties and grain growth in a CoCrFeMnNi high entropy alloy, Mat. Sci. Eng. 748 (2019) 228.
[19] Won-Mi. Choi Yong Hee Jo, Hyoung Seop Kim Seok Su Sohn, Sunghak Lee Byeong-Joo Lee, Role of brittle sigma phase in cryogenic-temperature-strength improvement of non-equi-atomic Fe-rich VCrMnFeCoNi high entropy alloys, Mat. Sci. Eng. 724 (2018) 403.
[20] S. Shuang, Q. Yu, X. Gao, Q.F. He, J.Y. Zhang, S.Q. Shi, Y. Yang, Tuning the microstructure for superb corrosion resistance in eutectic high entropy alloy, J. Mater. Sci. Technol. 109 (2022) 197–208.
[21] C. Wang, J. Yu, Y. Yu, Y. Zhao, Y. Zhang, X. Han, Comparison of the corrosion and passivity behavior between CrMnFeCoNi and CrFeCoNi coatings prepared by argon arc cladding, J. Mater. Res. Technol. 9 (4) (2020) 8482.
[22] Y.Z. Shi, J.K. Mo, F.Y. Zhang, B. Yang, P.K. Liaw, Y. Zhao, In-situ visualization of corrosion behavior of AlxCoCrFeNi high-entropy alloys during electrochemical polarization, J. Alloy. Compd. 844 (2020) 156014.
[23] X.L. Wan, A.D. Lan, M. Zhang, X. Jin, H.J. Yang, J.W. Qiao, Corrosion and passive behavior of Al0.8CrFeNi2.2 eutectic high entropy alloy in different media, J. Alloy. Compd. 944 (2023) 169217.
[24] Wenke Chai, Tao Lu, Ye Pan, Corrosion behaviors of FeCoNiCr$_x$(x= 0, 0.5, 1.0) multi-principal element alloys: Role of Cr-induced segregation, Intermetallics 116 (2020) 106654.
[25] Xing Wu Qiu, Chun-Ge Liu, Microstructure and properties of Al2CrFeCoCuTiNix high-entropy alloys prepared by laser cladding, J. Alloy. Compd. 553 (2013) 216–220.
[26] X. Wang, Y. Zhang, Microstructures and corrosion resistance properties of as-cast and homogenized AlFeNiCuCr high entropy alloy, Mater. Chem. Phys. 254 (2020) 123440.
[27] Ahmad Raza, Ho. Jin Ryu, Soon Hyung Hong, Strength enhancement and density reduction by the addition of Al in CrFeMoV based high-entropy alloy fabricated through powder metallurgy, Mater. Des. 157 (2018) 97–104.
[28] D.Y. Li, C.X. Li, T. Feng, Y.D. Zhang, G. Sha, John J. Lewandowski, Peter K. Liaw, Y. Zhang, High-entropy $Al_{0.3}$CoCrFeNi alloy fibers with high tensile strength and ductility at ambient and cryogenic temperatures, Acta Mater. 123 (2017) 285–294.
[29] Y. Chen, Q. Liu, L. Wang, et al., "Microstructure and mechanical properties of $Al_{0.3}$CoCrFeNi high entropy alloy under low temperature, Mater. Sci. Eng.: A 774 (2019).
[30] Z. Han, B. Zhang, J. Zhang, et al., Influence of grain size on the mechanical properties and fracture behavior of $Al_{0.3}$CoCrFeNi high-entropy alloy, Mater. Sci. Eng.: A 707 (2017) 686–691.
[31] F. Ye, Y. Yang, Y. Li, Y. Huang, T. Zhang, Z. Sun, Electrochemical corrosion behavior and mechanism of 316L stainless steel in H2SO4 solution with different concentrations, Corros. Sci. 181 (2021) 109269.
[32] K. Mohan, A. H, S.P. Vijayalakshmi, S. Aravindan, L. Amalraj, S.A. Antony, Improved corrosion resistance and mechanical properties of 316L stainless steel welds subjected to various post-weld heat treatments, Mater. Today.: Proc. 15 (2019) 239–244.
[33] N.G. Thompson, B.C. Syrett, Relationship between conventional pitting and protection potentials and a new, unique pitting potential, Corrosion 48 (1992) 649–659.
[34] L.L. Li, Z.B. Wang, Y.G. Zheng, Interaction between pitting corrosion and critical flow velocity for erosion-corrosion of 304 stainless steel under jet slurry impingement, Corros. Sci. 158 (2019) 108084.
[35] Sankara Papavinasam, 3-Electrochemical polarization techniques for corrosion monitoring. Woodhead Publishing Series in Metals and Surface Engineering, Woodhead Publishing, 2021, pp. 45–77.
[36] C.D. Taylor, S. Li, A.J. Samin, Oxidation versus salt-film formation: competitive adsorption on a series of metals from first-principles, Electrochim. Acta 269 (2018) 93–101.
[37] X.L. An, H. Zhao, T. Dai, H.G. Yu, Z.H. Huang, C. Guo, P.K. Chu, C.L. Chu, Effects of heat treatment on the microstructure and properties of cold-forged CoNiFe medium entropy alloy, Intermetallics 110 (2019) 106477.
[38] Z.Z. Li, S.T. Zhao, R.O. Ritchie, M.A. Meyers, Mechanical properties of high-entropy alloys with emphasis on face-centered cubic alloys, Prog. Mater. Sci. 102 (2019) 296–345.
[39] W. Zhang, Z.C. Ma, H.W. Zhao, L.Q. Ren, Breakthrough the strength-ductility trade-off in a high-entropy alloy at room temperature via cold rolling and annealing, Mater. Sci. Eng. A 800 (2021) 140264.
[40] P. Sathiyamoorthi, P. Asghari-Rad, J.W. Bae, H.S. Kim, Fine tuning of tensile properties in CrCoNi medium entropy alloy through cold rolling and annealing, Intermetallics 113 (2019) 106578.
[41] L. Lu, T. Zhu, Y. Shen, M. Dao, K. Lu, S. Suresh, Stress relaxation and the structure size-dependence of plastic deformation in nano twinned copper, Acta Mater. 57 (2009) 5165–5173.
[42] G. Laplanche, A. Kostka, C. Reinhart, J. Hunfeld, G. Eggeler, E.P. George, Reasons for the superior mechanical properties of medium-entropy CrCoNi compared to high-entropy CrMnFeCoNi, Acta Mater. 128 (2017) 292–303.
[43] Y.F. Kao, T.D. Lee, S.K. Chen, Y.S. Chang, Electrochemical passive properties of AlxCoCrFeNi(x=0, 0.25, 0.50, 1.00) alloys in sulfuric acids, Corros. Sci. 52 (2010) 1026–1034.
[44] C.C. Yen, H.N. Lu, M.H. Tsai, B.W. Wu, Y.-C. Lo, C.-C. Wang, S.-Y. Chang, S.-K. Yen, Corrosion mechanism of annealed equiatomic AlCoCrFeNi tri-phase high-entropy alloy in 0.5 M H2SO4 aerated aqueous solution, Corros. Sci. 157 (2019) 462–471.
[45] Yunzhu Shi, Bin Yang, Xie Xie, Jamieson Brechtl, Karin A. Dahmen, Peter K. Liaw, Corrosion of Al xCoCrFeNi high-entropy alloys: Al-content and potential scan-rate dependent pitting behavior, Corros. Sci. 119 (2017) 33–45.
[46] X. He, R.G. Song, D.J. Kong, Microstructure and corrosion behaviour of lasercladding Al-Ni-TiC-CeO2 composite coatings on S355 offshore steel, J. Alloy. Compd. 770 (2019) 771–783.
[47] A. Saraby-Reintjes, Theory of competitive adsorption and its application to the anodic dissolution of nickel and other iron-group metals-II. The steady state in the prepassive, passive and transpassive potential ranges, Electrochim. Acta 30 (1985) 403–417.
[48] J. Soltis, Passivity breakdown, pit initiation and propagation of pits in metallic materials - Review, Corros. Sci. 90 (2015) 5–22.
[49] S. Guiso, D. di Caprio, J. de Lamare, B. Gwinner, Intergranular corrosion: comparison between experiments and cellular automata, Corros. Sci. 177 (2020) 108953.
[50] Y.Z. Shi, L. Collins, N. Balke, P.K. Liaw, B. Yang, In-situ electrochemical-AFM study of localized corrosion of Al_xCoCrFeNi high-entropy alloys in chloride solution, Appl. Surf. Sci. 439 (2018) 533–544.
[51] S. Wang, Y.H. Zhao, X.T. Xu, P. Cheng, H. Hou, Evolution of mechanical properties and corrosion resistance of Al0.6CoFeNiCr0.4 high-entropy alloys at different heat treatment temperature, Mater. Chem. Phys. 244 (2020) 122700.
[52] Q.N. Song, Y.G. Zheng, D.R. Ni, Z.Y. Ma, Studies of the nobility of phases using scanning Kelvin probe microscopy and its relationship to corrosion behaviour of Ni–Al bronze in chloride media, Corros. Sci. 92 (2015) 95–103.